

# Lab on a Chip

Accepted Manuscript



This is an *Accepted Manuscript*, which has been through the Royal Society of Chemistry peer review process and has been accepted for publication.

*Accepted Manuscripts* are published online shortly after acceptance, before technical editing, formatting and proof reading. Using this free service, authors can make their results available to the community, in citable form, before we publish the edited article. We will replace this *Accepted Manuscript* with the edited and formatted *Advance Article* as soon as it is available.

You can find more information about *Accepted Manuscripts* in the [Information for Authors](#).

Please note that technical editing may introduce minor changes to the text and/or graphics, which may alter content. The journal's standard [Terms & Conditions](#) and the [Ethical guidelines](#) still apply. In no event shall the Royal Society of Chemistry be held responsible for any errors or omissions in this *Accepted Manuscript* or any consequences arising from the use of any information it contains.

## **Local redox cycling-based electrochemical chip device with nanocavities for multi-electrochemical evaluation of embryoid bodies**

Yusuke Kanno<sup>1</sup>, Kosuke Ino<sup>1</sup>, Hitoshi Shiku<sup>1</sup>, and Tomokazu Matsue<sup>1,2</sup>

<sup>1</sup> Graduate School of Environmental Studies, Tohoku University, Japan

<sup>2</sup> WPI-Advanced Institute for Materials Research, Tohoku University, Japan

Corresponding authors:

Kosuke Ino (ino.kosuke@bioinfo.che.tohoku.ac.jp)

Tomokazu Matsue (matsue@bioinfo.che.tohoku.ac.jp)

Keywords:

Electrode array

Electrochemical cell analysis

Nanocavity

Redox cycling

Embryonic stem cells

1    **Abstract**

2            An electrochemical device, which consists of electrode arrays, nanocavities, and  
3 microwells, was developed for multi-electrochemical detection with high sensitivity. A local redox  
4 cycling–based electrochemical (LRC-EC) system was used for multi-electrochemical detection and  
5 signal amplification. The LRC-EC system consists of  $n^2$  sensors with only  $2n$  bonding pads for  
6 external connection. The nanocavities fabricated in the sensor microwells enable significant  
7 improvement of the signal amplification compared with previous devices we have developed. The  
8 present device was successfully applied for evaluation of embryoid bodies (EBs) from embryonic  
9 stem (ES) cells via electrochemical measurements of alkaline phosphatase (ALP) activity in EBs. In  
10 addition, EBs were successfully trapped in the sensor microwells using dielectrophoresis (DEP)  
11 manipulation at the device, which led to high-throughput cell analysis. This device is considered to  
12 be useful for multi-electrochemical detection and imaging for bioassays including cell analysis.

13

## 14 Introduction

15 Electrochemical methods have been applied to bio/chemical assay devices because they  
16 afford a sensitive, miniaturized, easy-to-handle detection scheme, which is particularly required in  
17 sophisticated devices with high sensitivity and high throughput that are fabricated using  
18 micro/nanofabrication techniques. For example, micro/nanofluidic devices have been developed for  
19 electrochemical detection, where microfluidic chips with a band-electrode detector was used for  
20 faster and simpler on-site monitoring of chemical species in a capillary electrophoresis  
21 electrochemical (CE-EC) system.<sup>1</sup> Microfluidic chip devices also enable manipulation of  
22 biomaterials such as live cells, so that microfluidic electrochemical devices have also been applied  
23 for high-throughput cell analysis and as cell-based biosensors.<sup>2, 3</sup> For a highly sensitive  
24 electrochemical assay, several methods have been developed. For example, the sensitivity of  
25 electrochemical detection can be significantly improved using a redox cycling system<sup>4-20</sup> in which  
26 two sets of electrodes are located in close proximity to one another. A redox species generated at one  
27 electrode diffuses to the other electrode where electrochemical reaction regenerates the original  
28 species. Redox cycling between the two electrodes amplifies the electrochemical response.<sup>4, 5</sup> The  
29 amplification factor increases with a decrease in the distance between the electrodes; therefore,  
30 nanofabrication processes for nanofluidic/nanocavity electrochemical devices with redox cycling  
31 detection has received much attention. Nanocavities have been fabricated by layer-by-layer metal  
32 assembly with a thin sacrificial Cr layer, followed by the sacrificial etching of the Cr layer to prepare  
33 nanocavities between metal layers such as Au electrodes.<sup>6</sup> Application of appropriate potentials at  
34 these electrodes leads to reaction of the target molecules, such as catechol,<sup>6</sup> at these electrodes and  
35 redox cycling between the nanocavities is induced, which provides an amplified electrochemical  
36 current. Rassaei and coworkers reported that quinone as an enzymatic reaction product is localized  
37 in the confined space of a nanochannel in which efficient redox cycling also occurs, so that the  
38 sensor allows sensitive detection of product molecules generated by the enzyme in real time.<sup>8</sup>  
39 Excellent sensitivity can be achieved, by which Lemay and coworkers have reported the detection of  
40 single molecules using nanocavity devices.<sup>9, 12, 17</sup>

41 In addition, micro/nanofabrication techniques have been applied for the integration of  
42 many sensors into a single chip device to realize electrochemical multi-detection and imaging. Chip  
43 devices that consist of microelectrodes have also been used for electrochemical cell analysis.<sup>21-23</sup>  
44 However, it is difficult to prepare many sensors on a small chip due to the lack of space for lead  
45 connections and connector pads. Thus, we have previously reported a redox cycling-based  
46 electrochemical system to incorporate many sensors within a small space.<sup>24-31</sup> The system consists of  
47  $n$  column and  $n$  row electrodes to form  $n^2$  crossing points with  $2n$  bonding pads for external  
48 connection. Application of appropriate potentials at these electrodes induces redox cycling only at  
49 the desired crossing points, which allows the crossing points to be used as individual sensors. We

50 have designated this novel methodology as local redox cycling-based electrochemical (LRC-EC)  
51 detection. Thus,  $n^2$  sensors can be easily incorporated into a small chip device with only  $2n$  bonding  
52 pads for external connection. In our previous studies, comb-type interdigitated array (IDA)  
53 electrodes were incorporated at each sensor point of the device<sup>24-26</sup> to detect the electrochemical  
54 signal induced by redox cycling.<sup>32</sup> Cell differentiation of embryonic stem (ES) cells via their alkaline  
55 phosphatase (ALP) activity, which is known as an undifferentiation marker of ES cells, was  
56 successfully imaged using the LRC-EC device with IDA electrodes that had a typical 5  $\mu\text{m}$  gap  
57 between the electrode fingers.<sup>24</sup> The sensitivity can be improved using short-gap IDAs; however,  
58 fabrication of an IDA with nanometer size gaps is technically difficult. Therefore, nanocavity  
59 electrodes have been incorporated into the LRC-EC system to increase the redox cycling efficiency  
60 and thereby improve the signal amplification.

61 In the present study, nanocavities were fabricated in the LRC-EC devices for highly  
62 sensitive electrochemical detection. The gaps between the sensor electrodes for redox cycling was  
63 230 nm, which is considerably smaller than the 5  $\mu\text{m}$  gaps with our previous device.<sup>24, 25</sup> In addition,  
64 microwells were incorporated into the device to trap the embryoid bodies (EBs) of ES cells for stable  
65 analysis. The ALP activities of the trapped EBs were evaluated with the device based on the redox  
66 cycling in the nanocavities. In addition, dielectrophoresis (DEP) manipulation was applied to trap  
67 EBs in the microwells.

68

## 69 **Materials and Methods**

### 70 **Detection system**

71 The general architecture of the device and setup is displayed in Fig. 1A. The LRC-EC  
72 device consisted of 4 row and 4 column electrodes. Top and bottom ring electrodes were connected  
73 to the row and column electrodes, respectively, and these ring electrodes were placed at the  
74 individual crossing points of the row and bottom electrodes. The top and bottom ring electrodes were  
75 separated with nanocavities (230 nm height). A multichannel potentiostat (HA-1010 mM4, Hokuto  
76 Denko, Japan) was connected to these electrodes through a clip connector (CCNL-050-37-FRC,  
77 Yokowo, Japan) and a switching matrix (NI PXI-2529, National Instruments, USA). Voltage control  
78 and data collection were performed using a program written with LabVIEW (National Instruments).  
79 Microwell arrays of SU-8 were fabricated at the individual crossing points. Local redox cycling was  
80 induced only at the ring electrodes located at the designated cross points. A sample solution was  
81 introduced onto the sensor area, and an Ag/AgCl (sat. KCl) electrode as reference and counter  
82 electrodes was inserted into the solution.

83 EBs were introduced into a solution on the device to trap a single EB in a microwell (Fig.  
84 1B). *p*-Aminophenyl phosphate (PAPP) in a solution was catalytically hydrolyzed by alkaline  
85 phosphatase (ALP) on the EBs to yield *p*-aminophenol (PAP) which can then be detected using  
86 redox cycling (Fig. 1B).<sup>24</sup> Redox cycling of PAP and the oxidation product, *p*-quinone imine (QI),  
87 was measured by the device. For imaging, the electrochemical responses at the 16 sensor microwells  
88 were collected by sequentially changing the potential applied to the row and column electrodes.

89

### 90 **Device fabrication**

91 The device fabrication process is described in Fig. 2. Nanocavities were fabricated by  
92 etching of sacrificial Cr layers, according to previous studies.<sup>7-19</sup> Briefly, Ti/Pt was sputtered onto a  
93 glass substrate (Matsunami Glass Ind., Ltd., Japan) to fabricate the bottom ring electrodes (outer  
94 diameter: 195  $\mu\text{m}$ , inner diameter: 150  $\mu\text{m}$ ) connected to the column electrodes. The bottom ring  
95 electrodes were used as generator electrodes.<sup>33</sup> Cr was sputtered onto the column electrodes to  
96 prepare the sacrificial Cr layer. Cr/Pt was then sputtered to fabricate the top ring electrodes  
97 connected to the row electrodes. The top ring electrodes were used as collector electrodes.<sup>33</sup> The  
98 configuration of the metal layers was observed using a 3D laser scanning confocal microscope  
99 (VK-X200, Keyence, Japan). A SU-8 layer (50  $\mu\text{m}$  thick, SU-8 3050, Microchem Co., USA) was  
100 fabricated on the device to form 4 $\times$ 4 microwells (diameter: 150  $\mu\text{m}$ , depth: 50  $\mu\text{m}$ , center-to-center  
101 distance: 300  $\mu\text{m}$ ). The sacrificial Cr layers were then etched with a Cr etching solution (3%  
102 perchloric acid solution containing 0.12 M ammonium hexanitratocerate (IV)) to prepare  
103 nanocavities between the top and bottom ring electrodes. During the etching process, the column and  
104 row electrodes were connected with a digital voltmeter (Custom Corp. CDM-2000D, Japan), and the

105 resistance between these electrodes was monitored to evaluate the etching process (Fig. S1).

106

### 107 **Redox current simulation**

108 Redox currents from top and bottom ring electrodes were calculated using COMSOL  
109 Multiphysics (ver. 5.1, COMSOL, Inc., USA).<sup>24, 34, 35</sup> A three-dimensional model containing  
110 nanocavities, ring electrodes and microwells is described in Figs. S2 and S3. To simplify the  
111 calculation, lead electrodes were removed and simple ring electrodes were arranged (Figs. S2 and  
112 S3). Ferrocenemethanol (FcCH<sub>2</sub>OH) was used as a redox compound. For the detection of FcCH<sub>2</sub>OH,  
113 the electrochemical system is assumed to be a reversible one-electron reaction in the simulation. The  
114 initial concentration of FcCH<sub>2</sub>OH is set at 1.0 mM.<sup>36</sup> The diffusion coefficients of FcCH<sub>2</sub>OH and  
115 FcCH<sub>2</sub>OH<sup>+</sup> are set at  $7.0 \times 10^{-10}$  m<sup>2</sup>/s, which indicates that the sum of FcCH<sub>2</sub>OH and FcCH<sub>2</sub>OH<sup>+</sup>  
116 equal to the initial concentration of FcCH<sub>2</sub>OH in the space during electrochemical detection. The  
117 concentrations of FcCH<sub>2</sub>OH and FcCH<sub>2</sub>OH<sup>+</sup> at the electrodes during the electrochemical reaction are  
118 calculated using the Nernst equation. The standard electrode potential of the redox compound is set  
119 to 0.216 V.<sup>37</sup>

120 For cyclic voltammetry in redox cycling mode, the bottom electrode (generator) was  
121 scanned from 0.00 to 0.50 V at 100 mV/s, while the top electrode was held at 0.00 V. The collection  
122 efficiency was defined as the ratio of the cathodic currents at the collector electrodes to anodic  
123 currents at the generator electrodes when the potential of the generator electrodes reached 0.5 V. For  
124 amperometry in redox cycling mode, a bottom electrode (generator) was stepped to 0.50 V, while a  
125 top electrode was held at 0.00 V. The currents at 10 s were used for calculation of the signal  
126 amplification. The responses were acquired from these electrodes when the channel heights were  
127 changed from 230 nm to 30 μm. For amperometry in non-redox cycling mode, a ring electrode was  
128 prepared on the bottom of the microwell (Fig. S3), and the potential was stepped to 0.50 V. The  
129 currents at 100 s were then used for calculation of the signal amplification.

130

### 131 **Characterization of the device**

132 The electrochemical performance of the LRC-EC device with nanocavities was  
133 investigated using FcCH<sub>2</sub>OH. Sample solutions were introduced by pipetting after O<sub>2</sub> plasma ashing  
134 for the device. The column electrode was stepped from 0.00 to 0.50 V, while the other electrodes  
135 were held at 0.00 V. The connection of these electrodes is shown in Fig. S4. Redox cycling-based  
136 responses from FcCH<sub>2</sub>OH in a Tris-HCl buffer (pH 9.5) at the row electrodes were acquired to  
137 prepare a calibration curve for FcCH<sub>2</sub>OH from a single sensor.

138

### 139 **Cell culture**

140 Mouse ES cells (129/Sv) were cultured according to a previous report.<sup>24</sup> Briefly, ES cells

141 were cultured in Stem Medium (Dainippon Sumitomo Pharma, Japan) supplemented with 1 mM  
142 mouse leukemia inhibitory factor (mLIF) and 0.1 mM 2-mercaptoethanol, and the culture medium  
143 was changed every day. EBs were formed by the hanging drop method.<sup>38</sup> The ES cells were  
144 suspended in Stem Medium supplemented with 15% fetal bovine serum (FBS) and no mLIF. The  
145 suspension was introduced onto the cover of a culture dish to form 20  $\mu$ L droplets containing 500  
146 cells. The droplets were then hung from the dish cover and the culture dish was incubated for 1 day  
147 to form EBs. The EBs were introduced into the device using a capillary.

148

#### 149 **Electrochemical detection for ALP activity on EBs**

150 Tris-HCl solution (pH 9.5) containing 4.0 mM PAPP (LKT Laboratories, USA) and 2 mM  
151  $MgCl_2$  was introduced into the device, and the EBs were then introduced into the microwells on the  
152 device using a capillary under a microscope. For activation of ALP,  $MgCl_2$  was added. The  
153 detection scheme based on redox cycling for ALP detection is shown in Fig. 1B. PAPP is  
154 catalytically hydrolyzed by ALP on the EBs to yield PAP. PAP is oxidized at the bottom ring  
155 electrodes (generator, 0.30 V) and the oxidation product, QI, diffuses to the top ring electrodes  
156 (collector, -0.30 V). QI is then reduced back to PAP at the top ring electrodes (collector, -0.30 V) and  
157 diffuses back to the bottom ring electrodes to be reoxidized. The redox cycling between the top and  
158 bottom ring electrodes amplifies the electrochemical signal from PAP produced by ALP on the EBs.  
159 Figure S5 shows an imaging process for the detection of ALP activity on the EBs. Briefly,  
160 redox-cycling based electrochemical signals were sequentially acquired by application of appropriate  
161 potentials at these electrodes to complete detection at all sensors. Electrochemical detection was  
162 performed in a Faraday cage.

163

#### 164 **DEP for manipulation of EBs using the LRC-EC device with nanocavities**

165 For DEP manipulation, an indium tin oxide (ITO) electrode was mounted face-to-face onto  
166 the device with a 260  $\mu$ m thick spacer. The ITO electrode and the ring electrodes in the device were  
167 connected to a function generator (Hioki E.E. Co., Nagano, Japan). EBs in 0.2 M sucrose solution  
168 were introduced into the 260  $\mu$ m high interspace between the ITO substrate and the device.  
169 Alternating electric fields (10 MHz, 20  $V_{pp}$ ) of opposite phase were then applied to the ring  
170 electrodes and the ITO electrode, respectively. After manipulation of the EBs using DEP, 0.2 M  
171 sucrose solution was flowed in the interspace to remove excess EBs.

172



## 173 **Results and Discussion**

### 174 **Current simulation**

175 A cyclic voltammetry simulation for redox compounds was conducted to clarify the signal  
176 amplification, collection efficiency, cross-talk, and time to reach steady-state. The configuration of  
177 the electrodes used for the simulation is shown in Figs. 3A and S2. When the cavity height is set at  
178 20  $\mu\text{m}$ , the collector current from the top electrode and the generator current from the bottom  
179 electrode at 0.50 V were -37.2 and 46.6 nA, respectively, and the collection efficiency was 80% (Fig.  
180 3B). However, for a nanocavity height of 230 nm, the collector current from the top electrode and  
181 the generator current from the bottom electrode were -1.47 and 1.48  $\mu\text{A}$ , respectively, and the  
182 collection efficiency was approximately 100% (Fig. 3B). These results indicate that there is no  
183 crosstalk because the diffusion layer does not broaden during electrochemical detection when using  
184 a 230 nm gap. Figure 3C shows that the collector signals are inversely proportional to the nanocavity  
185 height. Thus, the collector currents are strictly dependent on the distance between the top and bottom  
186 electrodes. The collection efficiency increases with a decrease in the distance and reaches  
187 approximately 100% when the nanocavity height is 230 nm (Fig. 3D).

188 Figures 3E and 3F show the results for the amperometric simulation. The time to reach  
189 steady-state was significantly dependent on the channel height. With the nanocavities, the time to  
190 steady-state can be significantly shortened because a steady-state diffusion layer forms in the cavity  
191 within a short period. Therefore, the LRC-EC device with nanocavities can be applied for rapid  
192 electrochemical imaging.

193 When both the top and bottom electrodes are synchronously stepped to 0.50 V (non-redox  
194 cycling mode), redox compounds are consumed by the top and bottom electrodes, which causes  
195 depletion of the redox compounds in the cavity. As a result, the current decreases to background  
196 current. Therefore, the electrochemical current from a simple ring electrode was calculated and used  
197 as a reference value in non-redox cycling mode to evaluate the signal amplification of redox cycling  
198 in the device. The configuration of the simple ring electrodes is given in Fig. S3. From the  
199 amperometric simulation of the non-redox cycling condition, the current was approximately 15 nA at  
200 100 s (Fig. S3). In contrast, the current in redox cycling mode was approximately -1.5  $\mu\text{A}$  when  
201 using a 230 nm gap (Fig. 3E), which is almost 100 times larger than that for non-redox cycling mode.  
202 Thus, the system with nanocavities is useful for highly sensitive and rapid electrochemical assay.

203

### 204 **Device fabrication**

205 Figure 4 shows the process for device fabrication. The layer thicknesses of the present  
206 device were as follows; the first Ti/Pt layer, 70 nm (Fig. 4A); the second Cr layer, approximately 200  
207 nm (Fig. 4B); the third Cr/Pt layer, 130 nm (Fig. 4C). The total thickness of the sacrificial Cr  
208 between the top Pt and bottom Pt electrodes was 230 nm.

209 Figure 5A and Movie S1 show optical images during the etching process of the sacrificial  
210 Cr layer. After adding the Cr etching solution into the microwells, the sacrificial Cr layer was  
211 removed gradually. After etching for approximately 25 min, the resistance between the top and  
212 bottom electrodes increased sharply (Fig. 5B), which indicates complete removal of the Cr sacrificial  
213 layer between the ring electrodes. The percentage of functional structures fabricated with the etching  
214 process was 50 %, and the rest of the devices showed a short circuit. In addition, 30 % of the  
215 functional devices were suitable for redox cycling-based detection.

216 A silicon layer is also utilized for a sacrificial layer for nanofluidics.<sup>20, 39</sup> To remove the  
217 silicon sacrificial layer, reactive ion etching using SF<sub>6</sub> gas or etching solutions with high temperature  
218 are used. In contrast, we utilized a sacrificial chromium layer because the etching process is easily  
219 performed and allows high selectivity and a well-controlled etch rate. Materials for sensing  
220 electrodes should show proper adherence to chromium for layer-by-layer fabrication, which is the  
221 limitation when deciding the materials of the electrodes. Since Pt and Au meet the limitation, Pt was  
222 chosen in the present study.

223 Figure 6 shows optical images of the LRC-EC device with nanocavities. The device  
224 consisted of 16 electrochemical sensors and only 8 connector pads. The top and bottom ring  
225 electrodes were prepared at the crossing points, which were separated by the 230 nm high  
226 nanocavities. The center-to-center distance of the sensors was 300 μm. Microwells with 150 μm  
227 diameter and 50 μm depth were prepared at the crossing points to trap EBs.

228 The fabrication process for device with nanocavity is slightly complex, compared to our  
229 previous devices,<sup>24-31</sup> which is disadvantages.

230

### 231 **Calibration curve**

232 Chronoamperometry using the device demonstrated that redox cycling was rapidly  
233 established so that steady-state currents could be rapidly acquired (Fig. 7A). The electrochemical  
234 signals at the sensor were proportional to the concentration of FcCH<sub>2</sub>OH (Fig. 7B) and the detection  
235 limit of FcCH<sub>2</sub>OH was less than 100 nM; therefore, the device can be used for the quantitative  
236 detection of redox components in nanocavities. According to the calibration curve, the  
237 electrochemical signal for 1.0 mM FcCH<sub>2</sub>OH was estimated to be approximately -1.0 μA, which was  
238 approximately two-thirds of the simulation current (-1.5 μA). This discrepancy may be caused by  
239 fouling of the electrodes and/or deformation of the channels.

240 According to our previous work using interdigitated ring array (IDRA) electrodes with 5  
241 μm-gap electrodes, current density of a collector electrode was estimated to approximately 0.16  
242 pA/μm<sup>2</sup> from 10 μM FcCH<sub>2</sub>OH.<sup>30</sup> On the other hand, the current density was approximately 1.9  
243 pA/μm<sup>2</sup> (Fig. 7), which was 12 times higher than that of the previous device due to highly effective  
244 redox cycling in the nanocavity. Therefore, the device with the nanocavity was more sensitive than

245 the previous device.

246

### 247 **Electrochemical imaging of ALP activity in EBs**

248 Figure 8 shows an electrochemical image for ALP activity in EBs (ca. 150  $\mu\text{m}$  diameter).  
249 The electrochemical images follow the position of the EBs (Figs. 8B and 8C). When no PAPP was  
250 added to the solution, no electrochemical signals were acquired from the sensors with EBs. These  
251 results clearly demonstrate that the electrochemical signals were derived from the redox cycling of  
252 PAP/QI after catalytic hydrolysis of PAPP by ALP (Fig. 8D). PAPP was chosen because it is a  
253 common substrate for redox cycling-based detection of ALP and it is commercially available. Other  
254 substrates for electrochemical detection of ALP are described in Supporting Information.

255 We have previously reported that electrochemical methods can be applied for the  
256 evaluation of ES cell differentiation via their ALP activity.<sup>40</sup> The LRC-EC system is especially useful  
257 for multi-electrochemical detection of ES cell differentiation.<sup>24, 26, 29-31</sup> Furthermore, the present  
258 LRC-EC system is superior to our previous devices in terms of the sensitivity due to the efficient  
259 redox cycling in the nanocavities. In our previous paper,<sup>29</sup> IDRA electrodes with a 5- $\mu\text{m}$  gap was  
260 successfully applied for detection of EB differentiation. Current density of a collector electrode was  
261 approximately 1.9  $\text{pA}/\mu\text{m}^2$  from each EB that were fabricated by 1-day culture of 500 cells in a 20  
262  $\mu\text{L}$  droplet. In the present study, the current density was approximately 39  $\text{pA}/\mu\text{m}^2$ , which was 21  
263 times higher than that of the previous study. Therefore, the present device was more sensitive than  
264 previous devices due to highly effective redox cycling in the nanocavity.

265 According to the calibration curve (Fig. 7B) and the electrochemical image (Fig. 8), the  
266 PAP concentration on the sensors was estimated to be approximately 100  $\mu\text{M}$ , considering that the  
267 electrochemical systems are one- and two-electron reactions for  $\text{FcCH}_2\text{OH}$  and PAP, respectively.  
268 The estimated value is smaller than that in our previous studies (approximately 200-300  $\mu\text{M}$ ),<sup>24</sup>  
269 because the EBs were slightly further away from the sensors in the present study.

270 Although high pH will affect EB differentiation, high pH solution was used for ALP  
271 detection because the pH is suitable for ALP activity compared to neutral pH. We have reported  
272 electrochemical detection of ALP in neutral pH, and the electrochemical signals became 1/5 - 1/10.<sup>24,</sup>  
273 <sup>29</sup> Since electrochemical signals were sufficiently acquired in the present method, a neutral pH  
274 solution can be used for detection. Detection in neutral pH can provide no significant influence of  
275 cell viability and cell differentiation.

276 Since the detection limit of  $\text{FcCH}_2\text{OH}$  was less than 100 nM, the detection limit of PAP is  
277 estimated to less than 50 nM according to the number of transferred electrons in the reaction of  
278  $\text{FcCH}_2\text{OH}$  and PAP. Although single ALP molecules on EBs cannot be detected since ALP of EBs is  
279 not secreted ALP, there is some possibility of detecting single ALP molecules if ALP is introduced  
280 into the nanocavity.

281 The LRC-EC device can also be applied for the detection of neurotransmitters, such as  
282 dopamine, from dopaminergic cells. Dopamine is a key species for the treatment of Parkinson's  
283 disease;<sup>41</sup> therefore, highly sensitive detection of dopamine and related compounds will attract  
284 attention for cell-based therapy using dopaminergic cells.

285

### 286 **DEP for manipulation of EBs using the LRC-EC device with nanocavities**

287 DEP was reported by Pohl as the motion of dielectric particles under a non-uniform  
288 electric field.<sup>42</sup> DEP can be used to manipulate various particles, including non-charged particles, so  
289 that DEP techniques have been applied to separate, concentrate, or align target particles.<sup>43-51</sup> In the  
290 present study, the device was used to induce positive DEP (pDEP) for the preparation of EB arrays.  
291 Under pDEP, particles are moved to direction of strong electric field. Figure 9A shows the scheme  
292 for the manipulation of EBs using pDEP as the driving force. An AC electric field was applied  
293 between the ring electrodes in the device and the ITO substrate placed above the device. A  
294 non-uniform electric field was formed at the open space of the microwell, and the resulting pDEP  
295 force guided an EB into the microwell with the ring electrode and nanocavity (Fig. 9B and Movie  
296 S2). Only single EBs were trapped in the microwells because the size of the microwell was matched  
297 to the size of a single EB (Fig. 9B). Excess EBs were flushed away by introducing sucrose solution  
298 into the space. When the flushed EBs passed above empty microwells, they became trapped in the  
299 microwells due to DEP (Fig. 9B and Movie S2). The DEP effect was sufficiently strong to hold the  
300 EBs in the microwells under solution flow. Thus, a single EB array was easily fabricated using the  
301 DEP technique, which demonstrates the electrochemical system is useful for cell analysis.

302 We have previously reported that pDEP in a 0.2 M sucrose solution did not affect cell  
303 viability of HeLa cells.<sup>52</sup> Therefore, we assumed that a 0.2 M sucrose solution did not affect cell  
304 viability of ES cells. However, the previous paper showed that the DEP manipulation is not  
305 completely stress free, indicating that the DEP might affect cell differentiation of ES cells. Other  
306 study reported that cells are damaged at electric field strength of above 1 kV/cm.<sup>53</sup> We simulated the  
307 electric field strength on the device under DEP and confirmed that it is below 1 kV/cm around an EB  
308 (Fig. S6). These results also indicated that the DEP manipulation did not affect cell viability. The  
309 detailed influence of DEP for cell viability and cell differentiation is under investigation.

310 Wolfrun and colleagues reported nanocavities incorporated into an LRC-EC system,<sup>19</sup> and  
311 addressable detection was performed. In the present study, we have demonstrated that the LRC-EC  
312 device with nanocavities and microwells can be applied for the evaluation and manipulation of EBs,  
313 which suggests that the present system is useful for cell analysis.

314

### 315 **Conclusion**

316 An LRC-EC device with nanocavities and microwells was developed for

317 multi-electrochemical detection with high sensitivity. The nanocavities enable significant  
318 improvement of the signal amplification compared to our previous research. The LRC-EC device  
319 with nanocavities was successfully applied for the evaluation of EBs via their ALP activity. In  
320 addition, EBs were successfully trapped in the sensor microwells using DEP that was induced by the  
321 device, thereby enabling efficient cell analysis. The LRC-EC device is thus demonstrated to be  
322 useful for bioassays including cell analysis.

323

### 324 **Acknowledge**

325 This work was supported in part by a Grant-in-Aid for Scientific Research (A) (No.  
326 25248032), a Grant-in-Aid for Young Scientists (A) (No. 15H05415) and a Grant-in-Aid for  
327 challenging Exploratory Research (No. 26600057). This research was partly supported by Special  
328 Coordination Funds for Promoting Science and Technology, Creation of Innovation Centers for  
329 Advanced Interdisciplinary Research Areas Program from the Japan Science and Technology Agency.  
330 This study was also supported by the Asahi Glass Foundation. This work was also supported by a  
331 Grant-in-Aid of Tohoku University Institute for International Advanced Research and Education.

332

333

334 **References**

- 335 1. J. Wang, *Talanta*, 2002, **56**, 223-231.
- 336 2. K. Ino, Y. Kitagawa, T. Watanabe, H. Shiku, M. Koide, T. Itayama, T. Yasukawa and T. Matsue,  
337 *Electrophoresis*, 2009, **30**, 3406-3412.
- 338 3. T. Yasukawa, K. Nagamine, Y. Horiguchi, H. Shiku, M. Koide, T. Itayama, F. Shiraishi and T.  
339 Matsue, *Analytical Chemistry*, 2008, **80**, 3722-3727.
- 340 4. O. Niwa, M. Morita and H. Tabei, *Journal of Electroanalytical Chemistry*, 1989, **267**, 291-297.
- 341 5. K. Aoki, M. Morita, O. Niwa and H. Tabei, *Journal of Electroanalytical Chemistry*, 1988, **256**,  
342 269-282.
- 343 6. B. Wolfrum, M. Zevenbergen and S. Lemay, *Analytical Chemistry*, 2008, **80**, 972-977.
- 344 7. L. Rassaei, P. S. Singh and S. G. Lemay, *Analytical Chemistry*, 2011, **83**, 3974-3980.
- 345 8. L. Rassaei, K. Mathwig, S. Kang, H. A. Heering and S. G. Lemay, *ACS Nano*, 2014, **8**,  
346 8278-8284.
- 347 9. M. A. G. Zevenbergen, P. S. Singh, E. D. Goluch, B. L. Wolfrum and S. G. Lemay, *Nano*  
348 *Letters*, 2011, **11**, 2881-2886.
- 349 10. E. Kaetelhoe, B. Hofmann, S. G. Lemay, M. A. G. Zevenbergen, A. Offenhaeusser and B.  
350 Wolfrum, *Analytical Chemistry*, 2010, **82**, 8502-8509.
- 351 11. M. A. G. Zevenbergen, P. S. Singh, E. D. Goluch, B. L. Wolfrum and S. G. Lemay, *Analytical*  
352 *Chemistry*, 2009, **81**, 8203-8212.
- 353 12. P. S. Singh, E. Kaetelhoe, K. Mathwig, B. Wolfrum and S. G. Lemay, *ACS Nano*, 2012, **6**,  
354 9662-9671.
- 355 13. P. S. Singh, H.-S. M. Chan, S. Kang and S. G. Lemay, *Journal of the American Chemical*  
356 *Society*, 2011, **133**, 18289-18295.
- 357 14. S. Kang, K. Mathwig and S. G. Lemay, *Lab on a Chip*, 2012, **12**, 1262-1267.
- 358 15. M. Hueske, R. Stockmann, A. Offenhaeusser and B. Wolfrum, *Nanoscale*, 2014, **6**, 589-598.
- 359 16. E. Kaetelhoe, K. J. Krause, P. S. Singh, S. G. Lemay and B. Wolfrum, *Journal of the American*  
360 *Chemical Society*, 2013, **135**, 8874-8881.
- 361 17. S. Kang, A. F. Nieuwenhuis, K. Mathwig, D. Mampallil and S. G. Lemay, *ACS Nano*, 2013, **7**,  
362 10931-10937.
- 363 18. D. Mampallil, K. Mathwig, S. Kang and S. G. Lemay, *Analytical Chemistry*, 2013, **85**,  
364 6053-6058.
- 365 19. E. Kaetelhoe, D. Mayer, M. Banzet, A. Offenhaeusser and B. Wolfrum, *Beilstein Journal of*  
366 *Nanotechnology*, 2014, **5**, 1137-1143.
- 367 20. M. A. G. Zevenbergen, D. Krapf, M. R. Zuiddam and S. G. Lemay, *Nano Letters*, 2007, **7**,  
368 384-388.
- 369 21. L.-M. Li, W. Wang, S.-H. Zhang, S.-J. Chen, S.-S. Guo, O. Francais, J.-K. Cheng and W.-H.

- 370 Huang, *Analytical Chemistry*, 2011, **83**, 9524-9530.
- 371 22. K. Hayashi, T. Horiuchi, R. Kurita, K. Torimitsu and O. Niwa, *Biosensors & Bioelectronics*,  
372 2000, **15**, 523-529.
- 373 23. N. Kasai, C. X. Han and K. Torimitsu, *Sensors and Actuators B-Chemical*, 2005, **108**, 746-750.
- 374 24. K. Ino, T. Nishijo, T. Arai, Y. Kanno, Y. Takahashi, H. Shiku and T. Matsue, *Angewandte*  
375 *Chemie-International Edition*, 2012, **51**, 6648-6652.
- 376 25. K. Ino, W. Saito, M. Koide, T. Umemura, H. Shiku and T. Matsue, *Lab on a Chip*, 2011, **11**,  
377 385-388.
- 378 26. K. Ino, Y. Kanno, T. Nishijo, T. Goto, T. Arai, Y. Takahashi, H. Shiku and T. Matsue, *Chemical*  
379 *Communications*, 2012, **48**, 8505-8507.
- 380 27. M. Sen, K. Ino, H. Shiku and T. Matsue, *Lab on a Chip*, 2012, **12**, 4328-4335.
- 381 28. K. Ino, T. Goto, Y. Kanno, K. Y. Inoue, Y. Takahashi, H. Shiku and T. Matsue, *Lab on a Chip*,  
382 2014, **14**, 787-794.
- 383 29. K. Ino, T. Nishijo, Y. Kanno, F. Ozawa, T. Arai, Y. Takahashi, H. Shiku and T. Matsue,  
384 *Electrochemistry*, 2013, **81**, 682-687.
- 385 30. K. Ino, T. Nishijo, Y. Kanno, H. Shiku and T. Matsue, *ECS Transactions*, 2013, **50**, 205-210.
- 386 31. K. Ino, Y. Kanno, T. Nishijo, H. Komaki, Y. Yamada, S. Yoshida, Y. Takahashi, H. Shiku and T.  
387 Matsue, *Analytical Chemistry*, 2014, **86**, 4016-4023.
- 388 32. O. Niwa, Y. Xu, H. B. Halsall and W. R. Heineman, *Analytical Chemistry*, 1993, **65**,  
389 1559-1563.
- 390 33. O. Niwa, M. Morita and H. Tabei, *Analytical Chemistry*, 1990, **62**, 447-452.
- 391 34. Y. Kanno, T. Goto, K. Ino, K. Y. Inoue, Y. Takahashi, H. Shiku and T. Matsue, *Analytical*  
392 *Sciences*, 2014, **30**, 305-309.
- 393 35. Y. Kanno, K. Ino, K. Y. Inoue, M. Sen, A. Suda, R. Kunikata, M. Matsudaira, H. Abe, C.-Z. Li,  
394 H. Shiku and T. Matsue, *Journal of Electroanalytical Chemistry*, 2015, **741**, 109-113.
- 395 36. C. Cannes, F. Kanoufi and A. J. Bard, *Journal of Electroanalytical Chemistry*, 2003, **547**,  
396 83-91.
- 397 37. A. Harper and M. R. Anderson, *Sensors*, 2010, **10**, 8248-8274.
- 398 38. H. Kurosawa, T. Imamura, M. Koike, K. Sasaki and Y. Amano, *Journal of Bioscience and*  
399 *Bioengineering*, 2003, **96**, 409-411.
- 400 39. M. Foquet, J. Korlach, W. Zipfel, W. W. Webb and H. G. Craighead, *Analytical Chemistry*, 2002,  
401 **74**, 1415-1422.
- 402 40. R. Obregon, Y. Horiguchi, T. Arai, S. Abe, Y. Zhou, RyosukeTakahashi, A. Hisada, K. Ino, H.  
403 Shiku and T. Matsue, *Talanta*, 2012, **94**, 30-35.
- 404 41. W. Dauer and S. Przedborski, *Neuron*, 2003, **39**, 889-909.
- 405 42. H. A. Pohl, *Journal of Applied Physics*, 1951, **22**, 869-871.

- 406 43. T. Yasukawa, H. Hatanaka and F. Mizutani, *Analytical Chemistry*, 2012, **84**, 8830-8836.
- 407 44. J. Ramon-Azcon, S. Ahadian, M. Estili, X. Liang, S. Ostrovidov, H. Kaji, H. Shiku, M.
- 408 Ramalingam, K. Nakajima, Y. Sakka, A. Khademhosseini and T. Matsue, *Advanced Materials*,
- 409 2013, **25**, 4028-4034.
- 410 45. D. R. Albrecht, R. L. Sah and S. N. Bhatia, *Biophysical Journal*, 2004, **87**, 2131-2147.
- 411 46. D. R. Albrecht, G. H. Underhill, T. B. Wassermann, R. L. Sah and S. N. Bhatia, *Nature Methods*,
- 412 2006, **3**, 369-375.
- 413 47. L. J. Yang, P. P. Banada, M. R. Chatni, K. S. Lim, A. K. Bhunia, M. Ladisch and R. Bashir, *Lab*
- 414 *on a Chip*, 2006, **6**, 896-905.
- 415 48. C.-T. Ho, R.-Z. Lin, W.-Y. Chang, H.-Y. Chang and C.-H. Liu, *Lab on a Chip*, 2006, **6**,
- 416 724-734.
- 417 49. Doh and Y. H. Cho, *Sensors and Actuators a-Physical*, 2005, **121**, 59-65.
- 418 50. N. Mittal, A. Rosenthal and J. Voldman, *Lab on a Chip*, 2007, **7**, 1146-1153.
- 419 51. N. Matsumoto, T. Matsue and I. Uchida, *Bioelectrochemistry and Bioenergetics*, 1994, **34**,
- 420 199-202.
- 421 52. T. Murata, T. Yasukawa, H. Shiku and T. Matsue, *Biosensors & Bioelectronics*, 2009, **25**,
- 422 913-919.
- 423 53. P. Bajaj, D. Marchwiany, C. Duarte and R. Bashir, *Advanced Healthcare Materials*, 2013, **2**,
- 424 450-458.
- 425



**426 Figure 1**

427 General outline of the LRC-EC device with nanocavities and microwells. (A) Illustration of the  
428 detection system. The device consists of 4 row electrodes containing top ring electrodes (blue) and 4  
429 column electrodes containing bottom ring electrodes (red). These ring electrodes are placed at the  
430 individual crossing points. The microwell arrays are fabricated at the individual crossing points, and  
431 the top and bottom ring electrodes are separated by nanocavities (230 nm height). Redox cycling is  
432 locally induced at the designated crossing points. (B) Detection scheme for ALP activity in EBs. EBs  
433 are trapped in microwells filled with PAPP and the enzymatic product by ALP, PAP, is measured.  
434 Electrochemical signals for the redox cycling of PAP/QI are acquired.

435

**436 Figure 2**

437 Schematic illustration of the device fabrication process. (i) Ti/Pt is sputtered onto a glass substrate to  
438 fabricate the column electrodes that contain the bottom ring electrodes. (ii) A sacrificial Cr layer is  
439 sputtered on the bottom ring electrodes. (iii) Cr/Pt is then sputtered to fabricate the row electrodes  
440 that contain the top ring electrodes. (iv) A SU-8 layer is fabricated on the device to form 4×4  
441 microwells (diameter: 150 μm, depth: 50 μm, gap: 300 μm). (v) The Cr sacrificial layer is etched to  
442 prepare nanocavities between the top and bottom ring electrodes.

443

**444 Figure 3**

445 Cyclic voltammograms and chronoamperograms obtained for the top and bottom ring electrodes  
446 using simulation software. (A) Illustration of the simulation model consisting of top and bottom  
447 electrodes. The top and bottom electrodes are used as collector and generator electrodes, respectively.  
448 The detailed configuration is shown in Fig. S2. The nanocavity heights were 230 nm to 30 μm. The  
449 nanocavity is filled with 1.0 mM FcCH<sub>2</sub>OH solution. (B) Cyclic voltammograms for nanocavity  
450 heights of 230 nm and 20 μm. The potential of the bottom ring electrode was scanned from 0.00 to  
451 0.50 V at 100 mV/s while the potential of the top ring electrode was kept at 0.00 V. (C) Currents in  
452 the cyclic voltammograms measured at 0.50 V. (D) Collection efficiency in the cyclic  
453 voltammograms measured at 0.50 V. (E) Chronoamperograms for nanocavity heights of 230 nm and  
454 20 μm. The potential of the bottom ring electrode was stepped to 0.50 V while the potential of the  
455 top ring electrode was kept at 0.00 V. (F) Time to reach steady-state current (99.9% of the reduction  
456 currents at 10 s) for nanocavity heights from 230 nm to 30 μm.

457

**458 Figure 4**

459 Configuration of the metal layers in each fabrication process. Three-dimensional (3D) topographies  
460 of (A) the first layer of Ti/Pt, (B) the second layer of Cr, and (C) the third layer of Cr/Pt. Heights of  
461 the metal layers and cross-sectional illustrations.

462

463 **Figure 5**

464 Time-course images of the device during etching of the sacrificial Cr layer. (A) Optical images. (B)  
465 Time-course analysis for the resistance between the top and bottom electrodes during the etching  
466 process. The movie for this process is shown in Movie S1.

467

468 **Figure 6**

469 Optical images of the LRC-EC device with nanocavities and microwells, and cross-sectional  
470 diagrams of the device.

471

472 **Figure 7**

473 Dependence of the electrochemical signals on the  $\text{FcCH}_2\text{OH}$  concentration. (A)  
474 Chronoamperograms at row electrodes where the potential was kept at 0.00 V while the column  
475 electrodes were stepped from 0.00 to 0.50 V. The connections of these electrodes are shown in Fig.  
476 S4. (B) Calibration curve. The currents were obtained from the row electrodes. The currents at 60 s  
477 were subtracted from those at 9.96 s for the background-corrected currents, and these values were  
478 plotted on a graph ( $N = 3$ ).

479

480 **Figure 8**

481 Electrochemical imaging of ALP activity in EBs. (A) Hanging droplets (500 cells, 20  $\mu\text{L}$ ) were  
482 incubated for 1 day to prepare EBs with approximately 150  $\mu\text{m}$  diameters. (B) Optical image of the  
483 EBs on the device. (C) Electrochemical image of ALP activity in EBs. The electrochemical signals  
484 were derived from redox cycling-based reaction of PAP, which is the enzymatic product of ALP  
485 reaction in EBs. (D) The currents were plotted on a graph ( $N = 3$ ).

486

487 **Figure 9**

488 Manipulation of EBs using DEP. (A) Scheme for the capture of EBs using DEP. (B) Optical images  
489 of EBs on the device during DEP manipulation and fluidic manipulation. The movie for this process  
490 is shown in Movie S2.

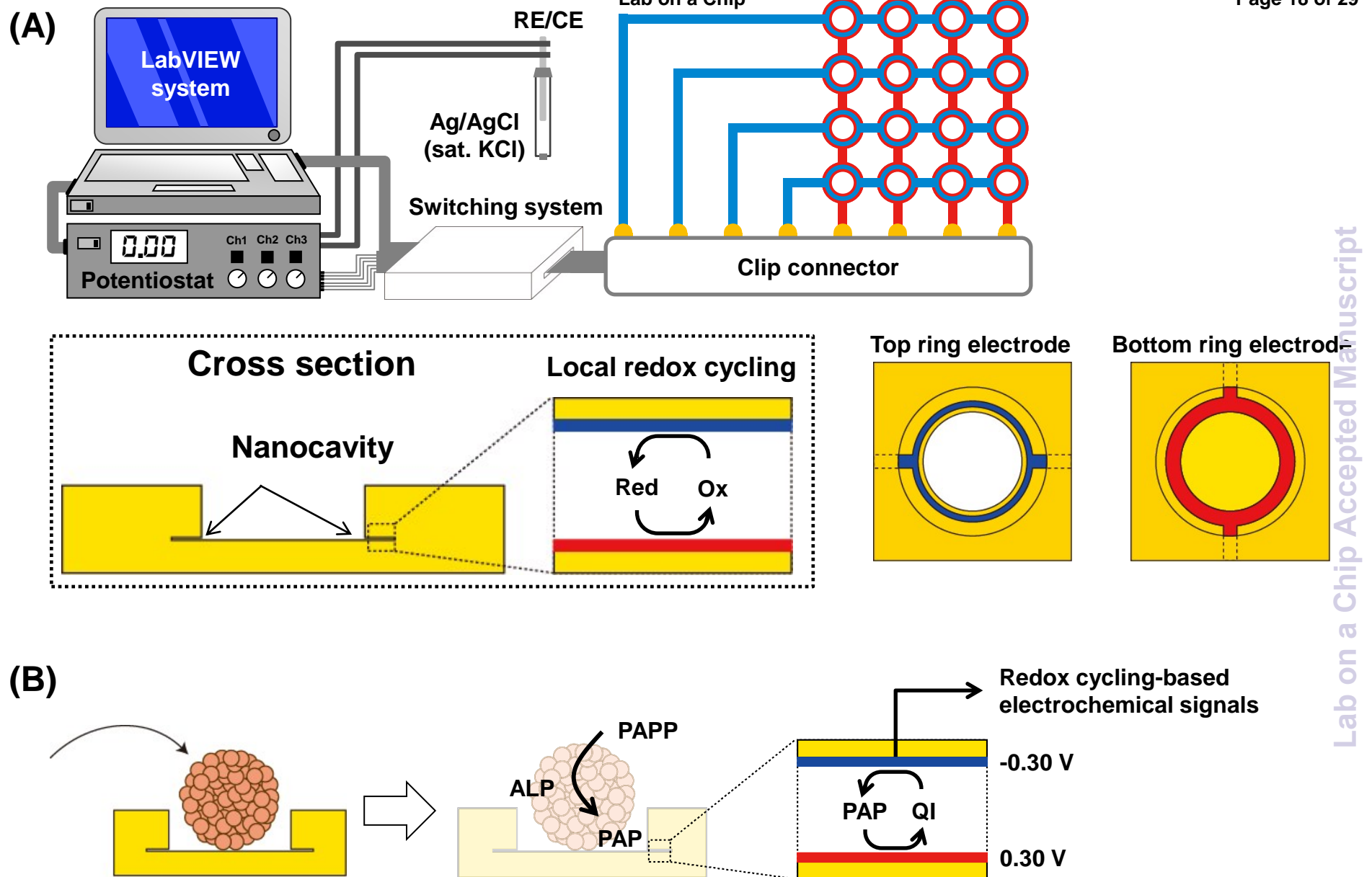
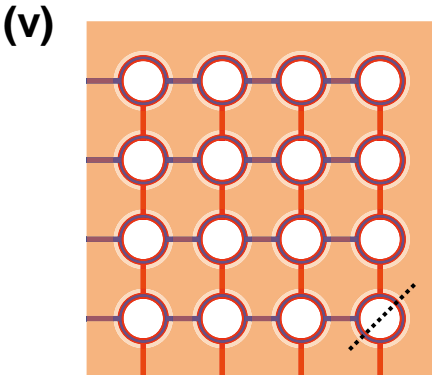
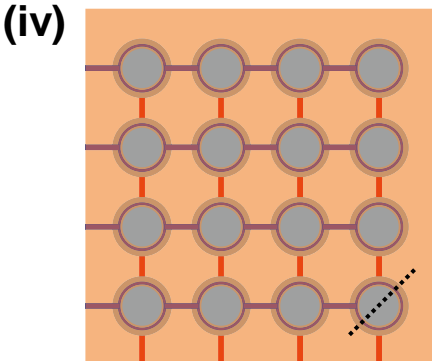
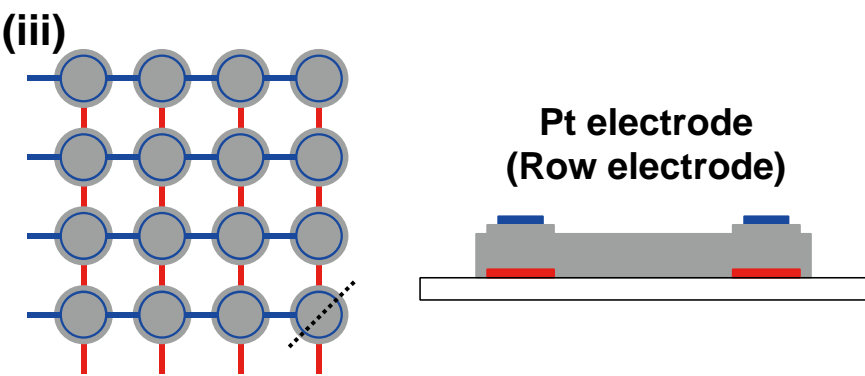
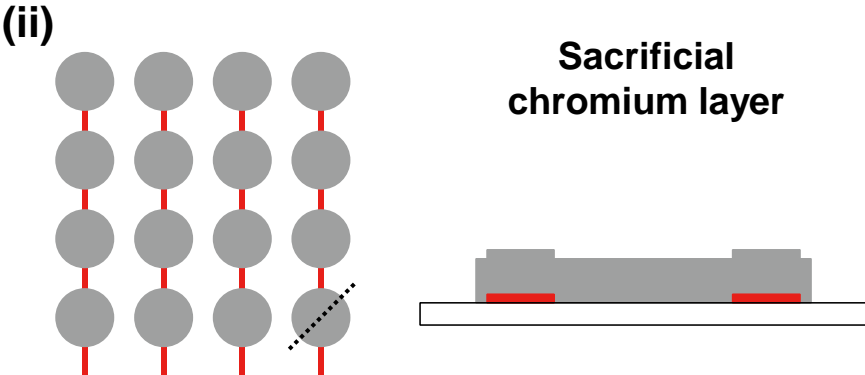
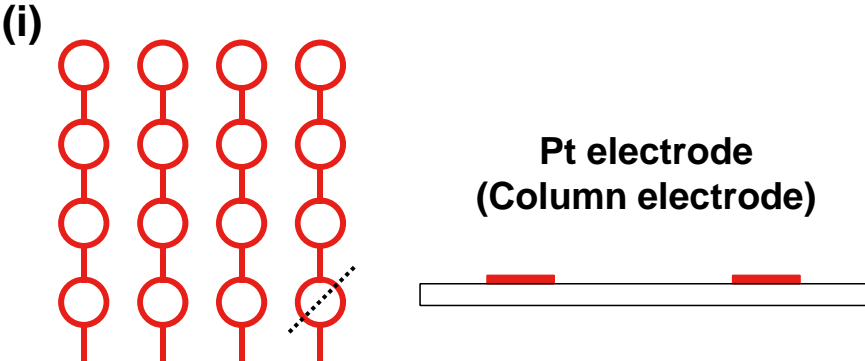


Figure 1



Lab on a Chip Accepted Manuscript

Figure 2

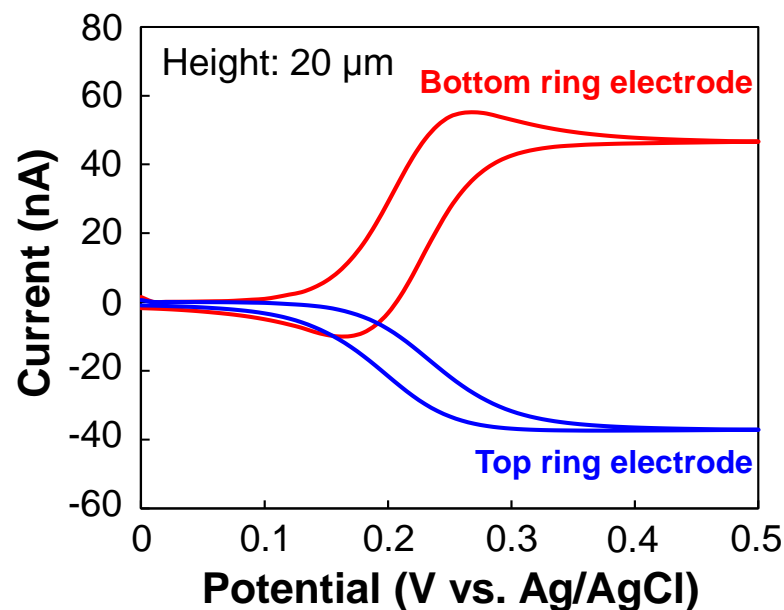
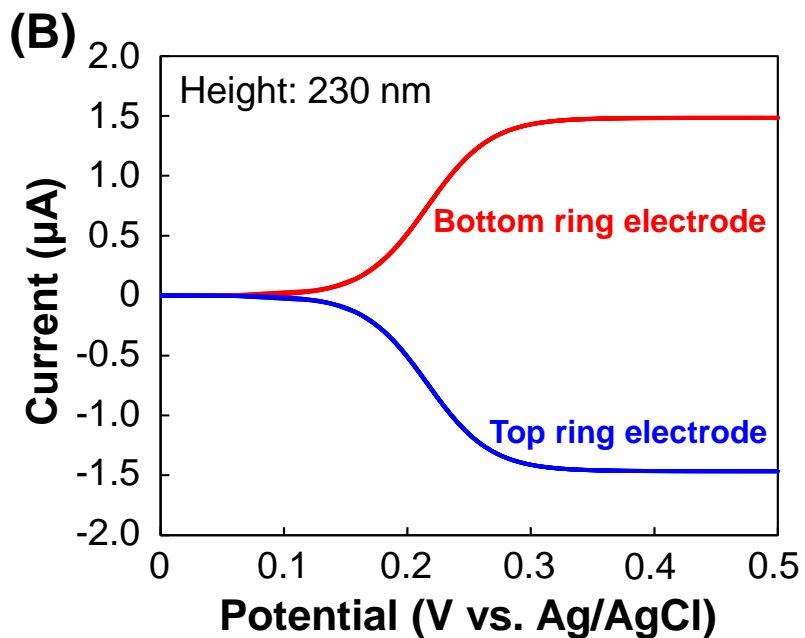
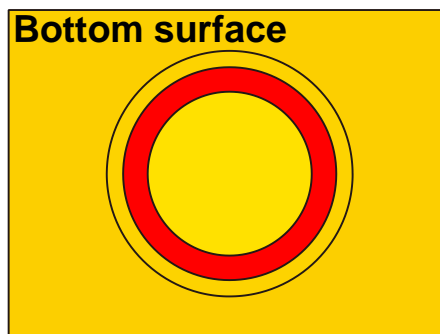
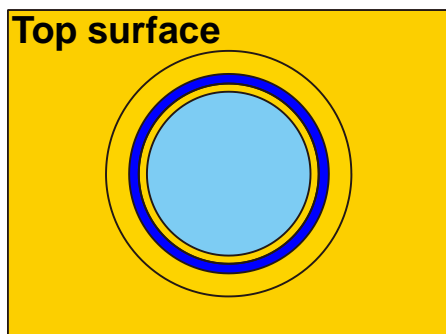
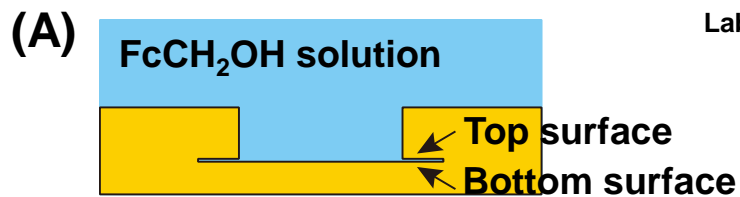


Figure 3A-3B

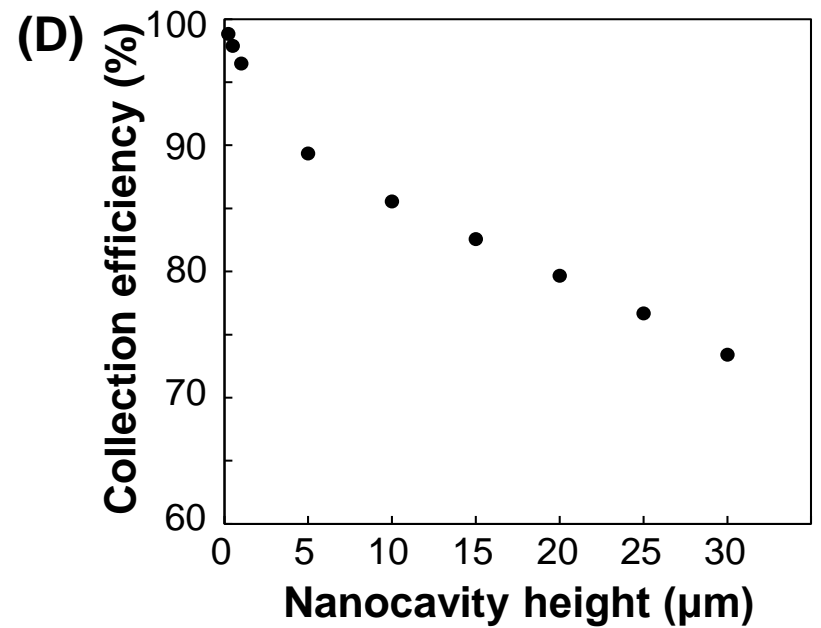
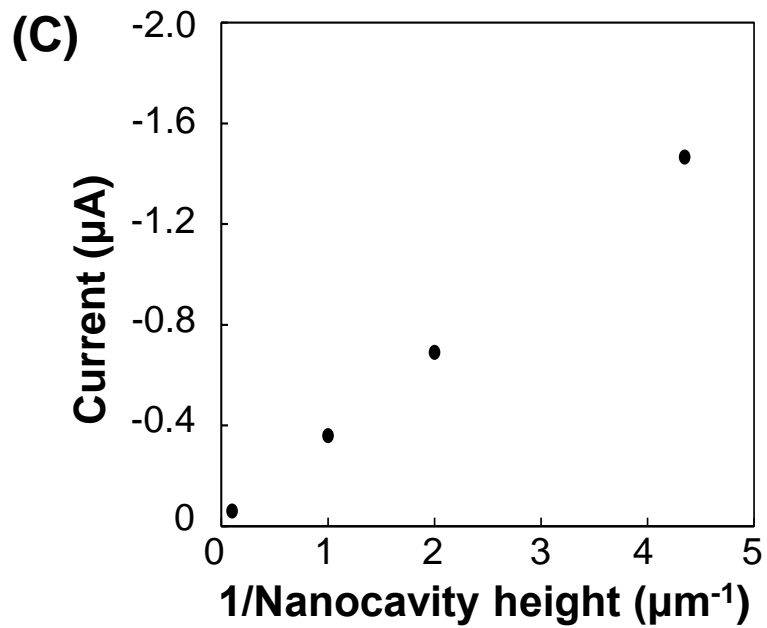
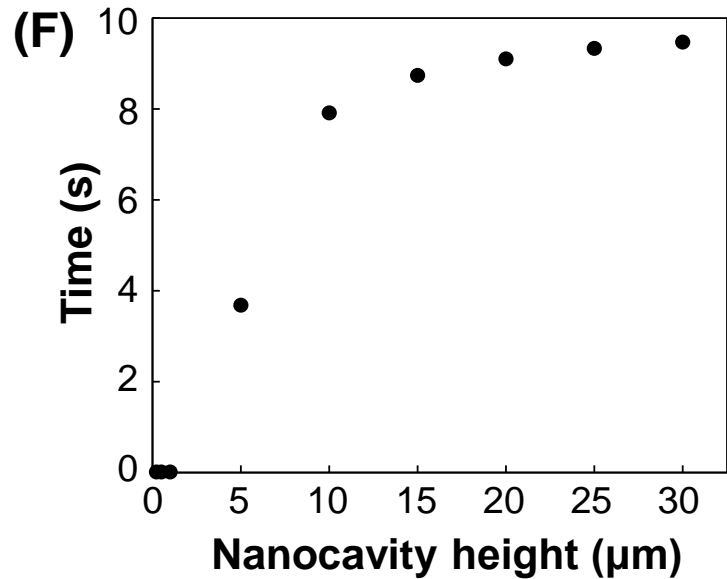
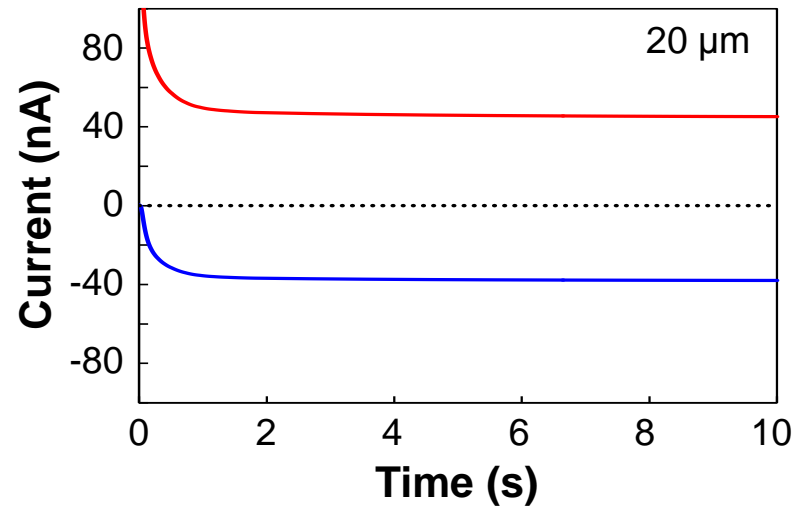
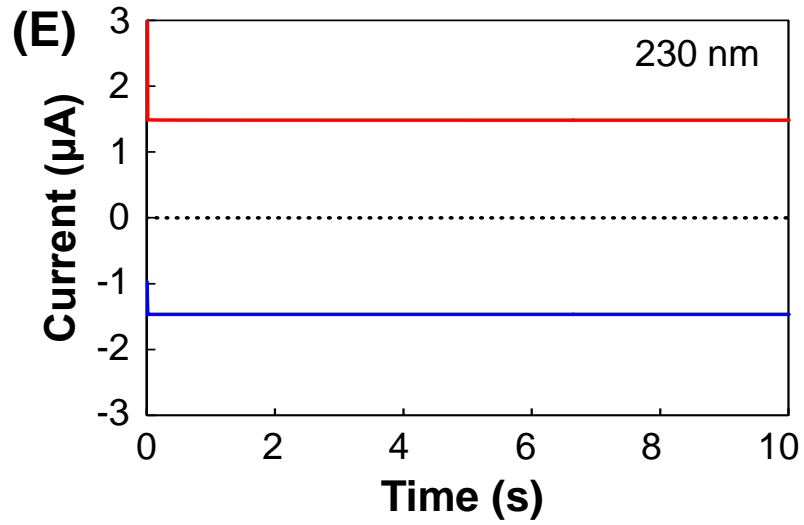
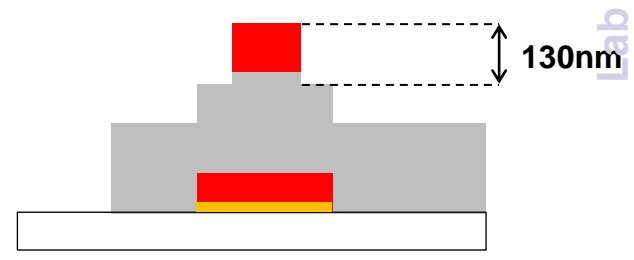
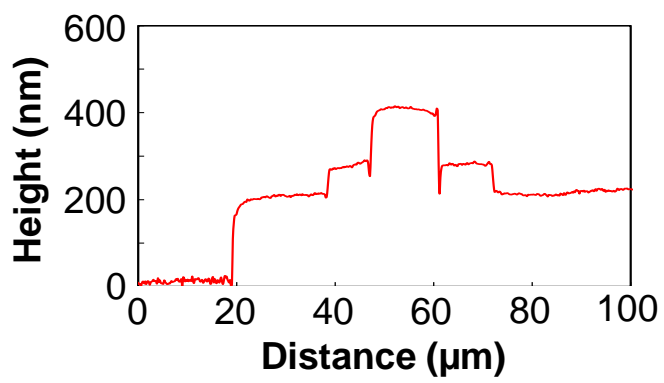
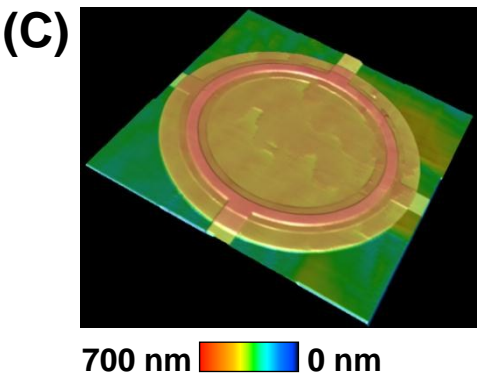
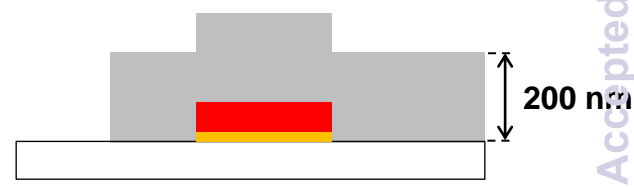
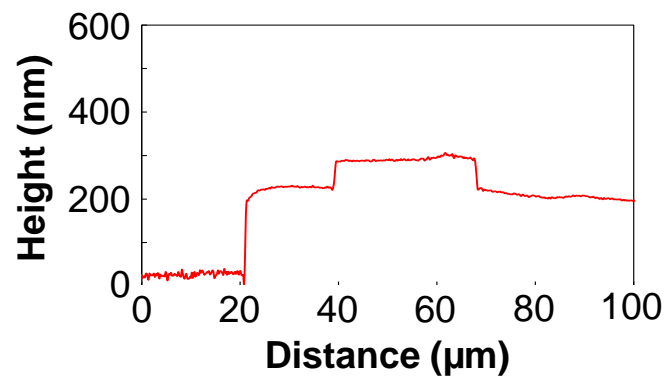
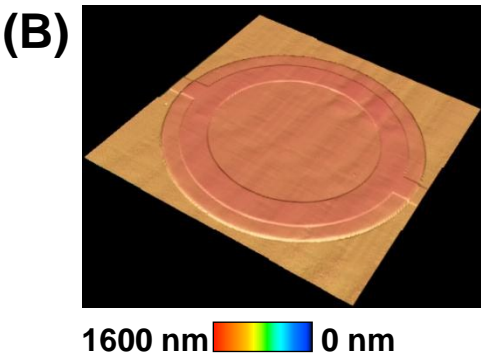
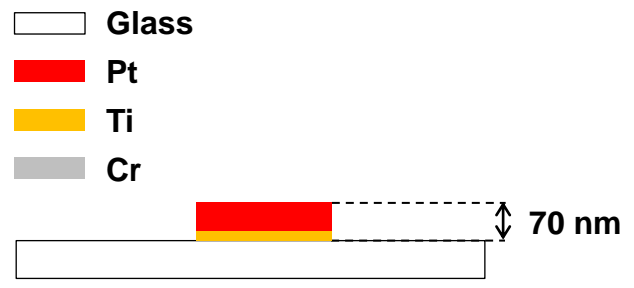
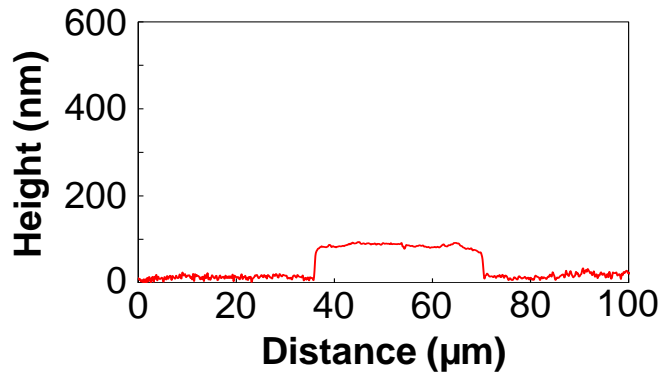
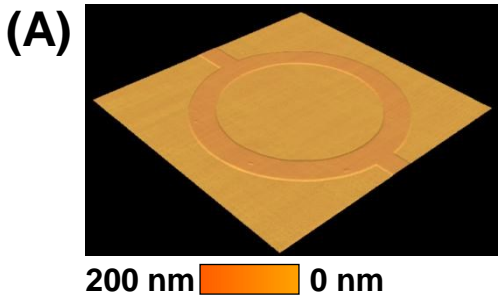


Figure 3C-3D



Lab on a Chip



Lab on a Chip Accepted Manuscript

Figure 4



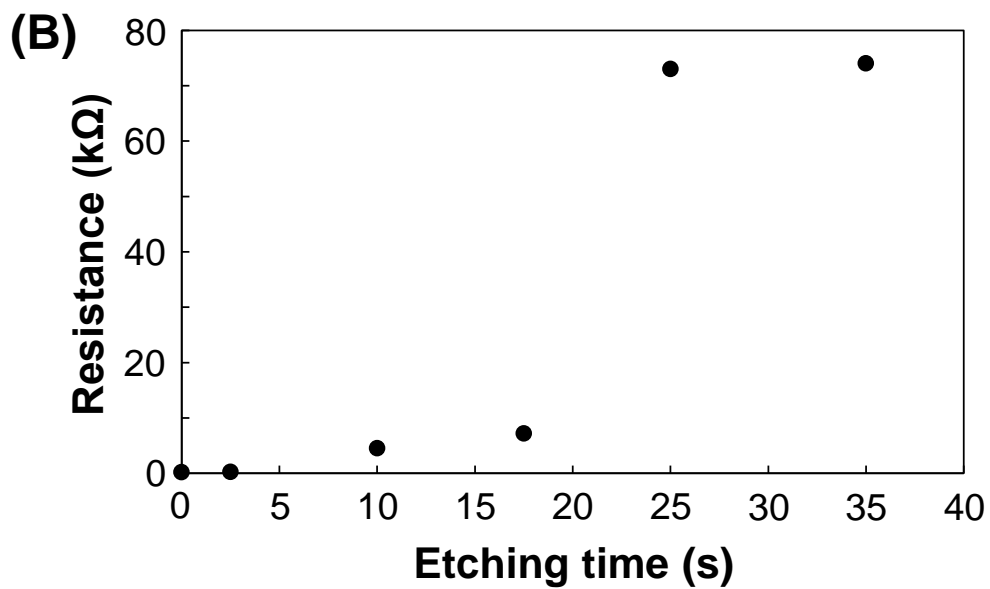
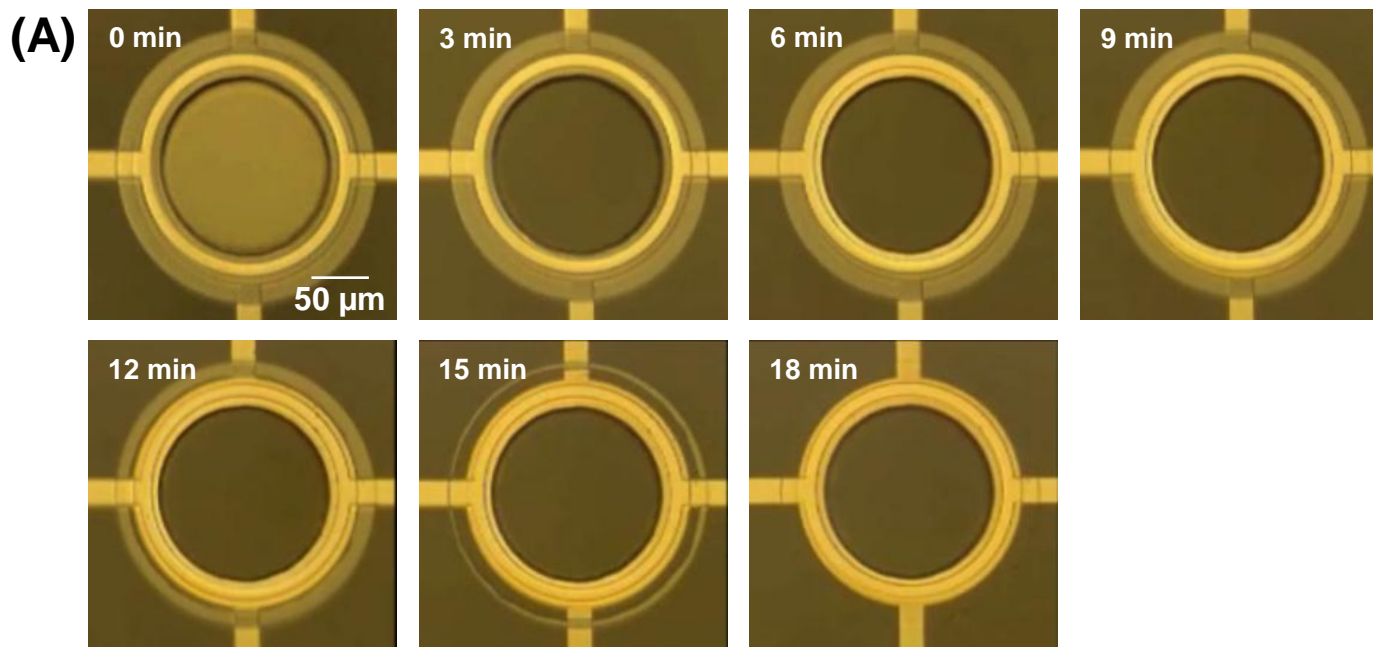


Figure 5

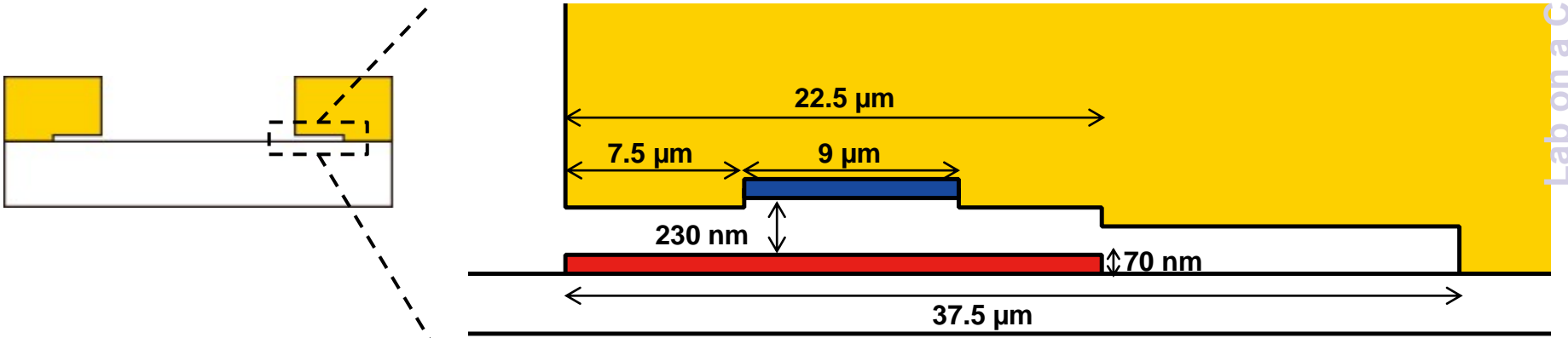
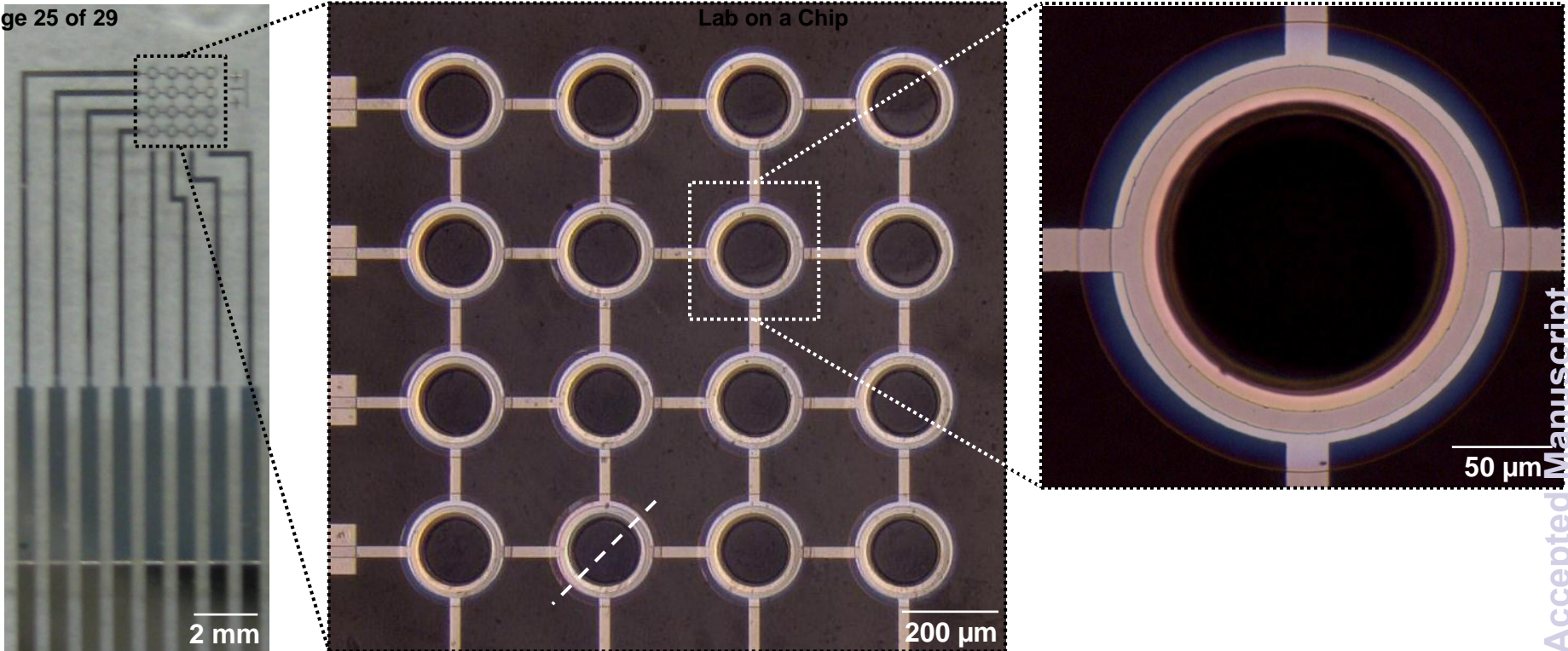


Figure 6

Lab on a Chip Accepted Manuscript

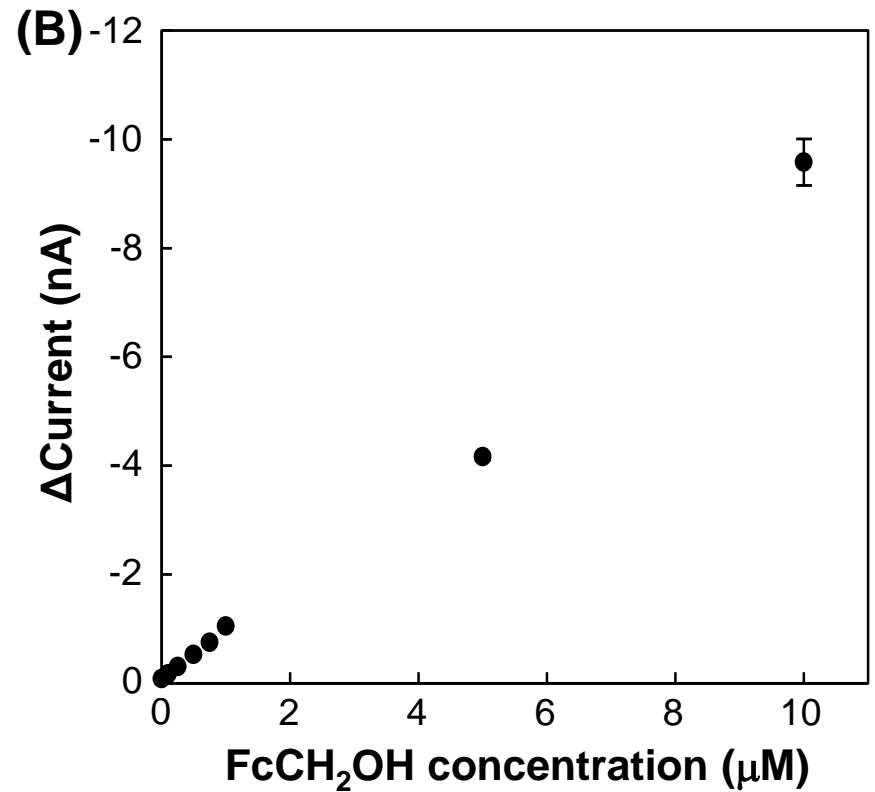
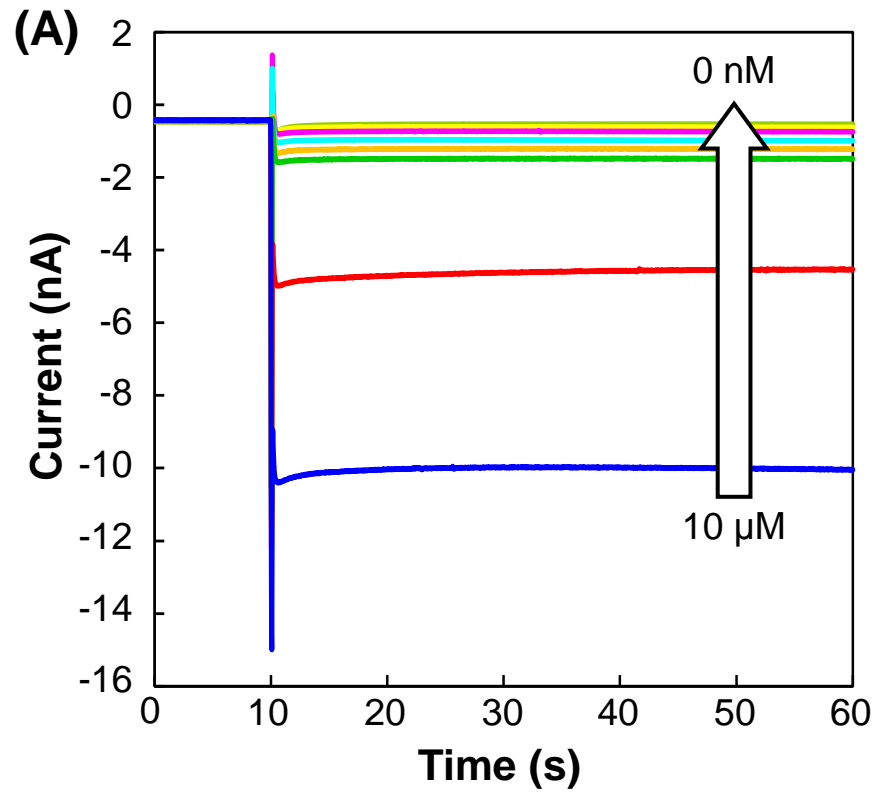
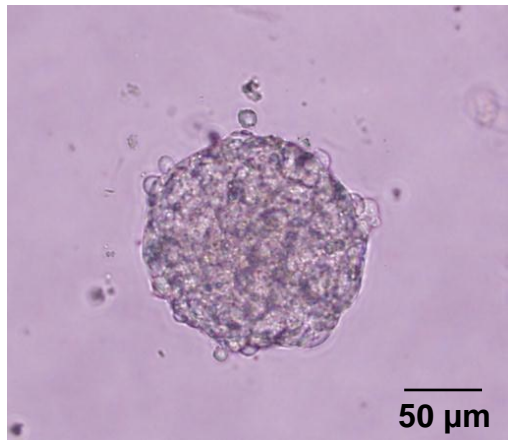
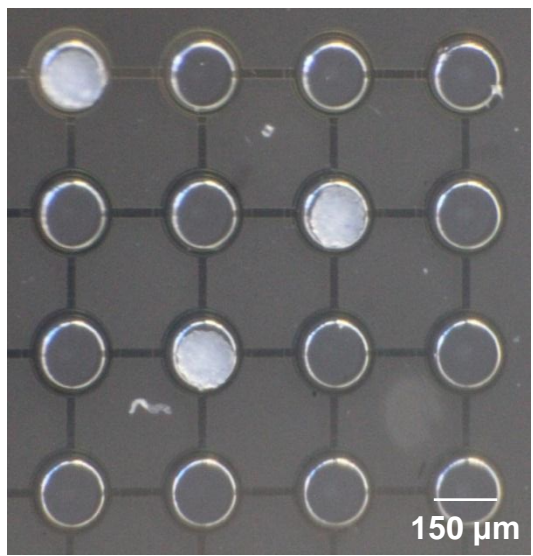


Figure 7

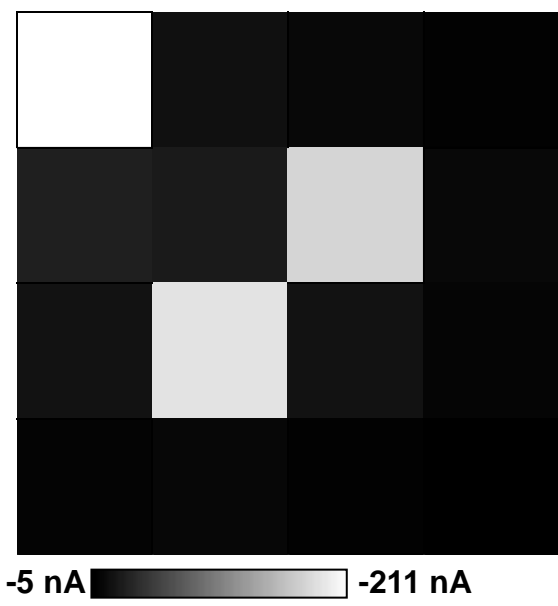
(A)



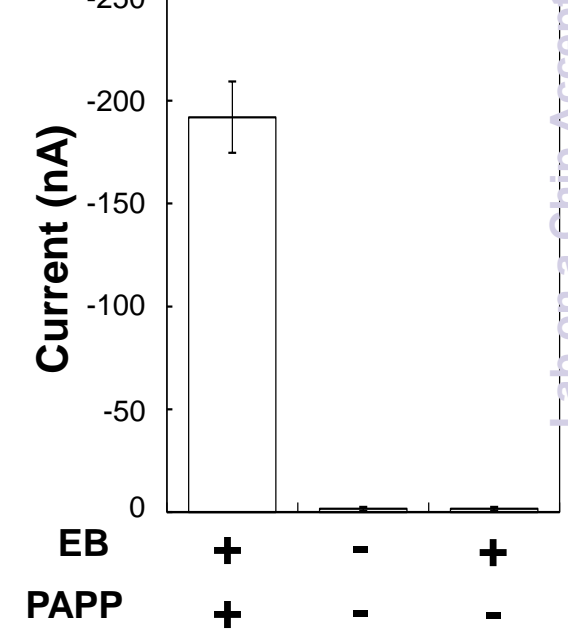
(B)



(C)

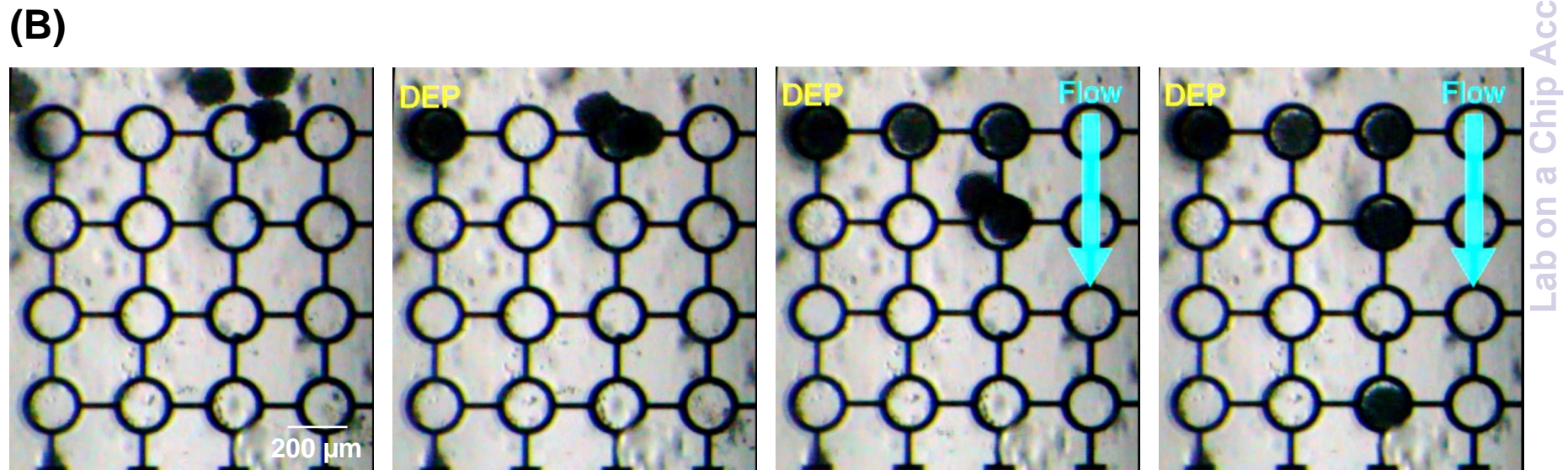
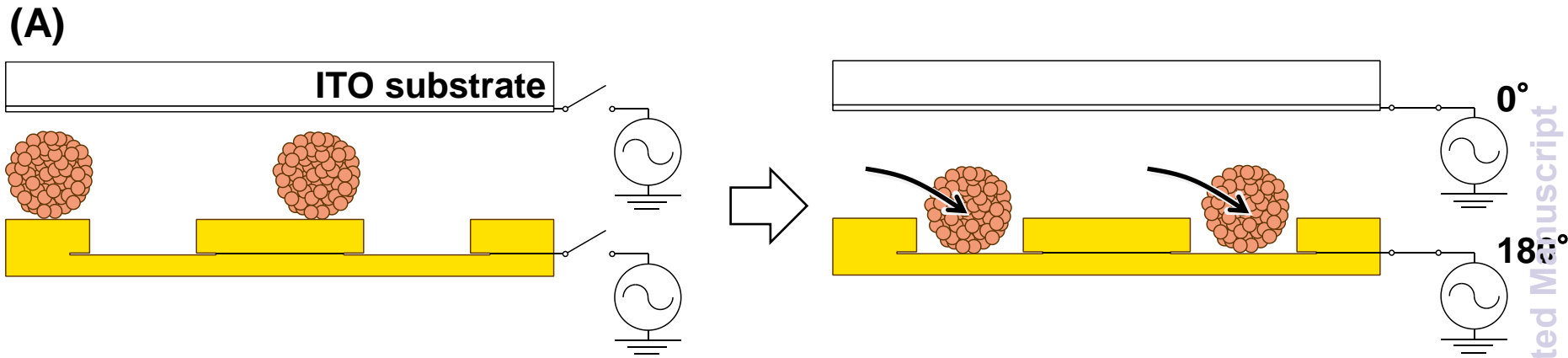


(D)



Lab on a Chip Accepted Manuscript

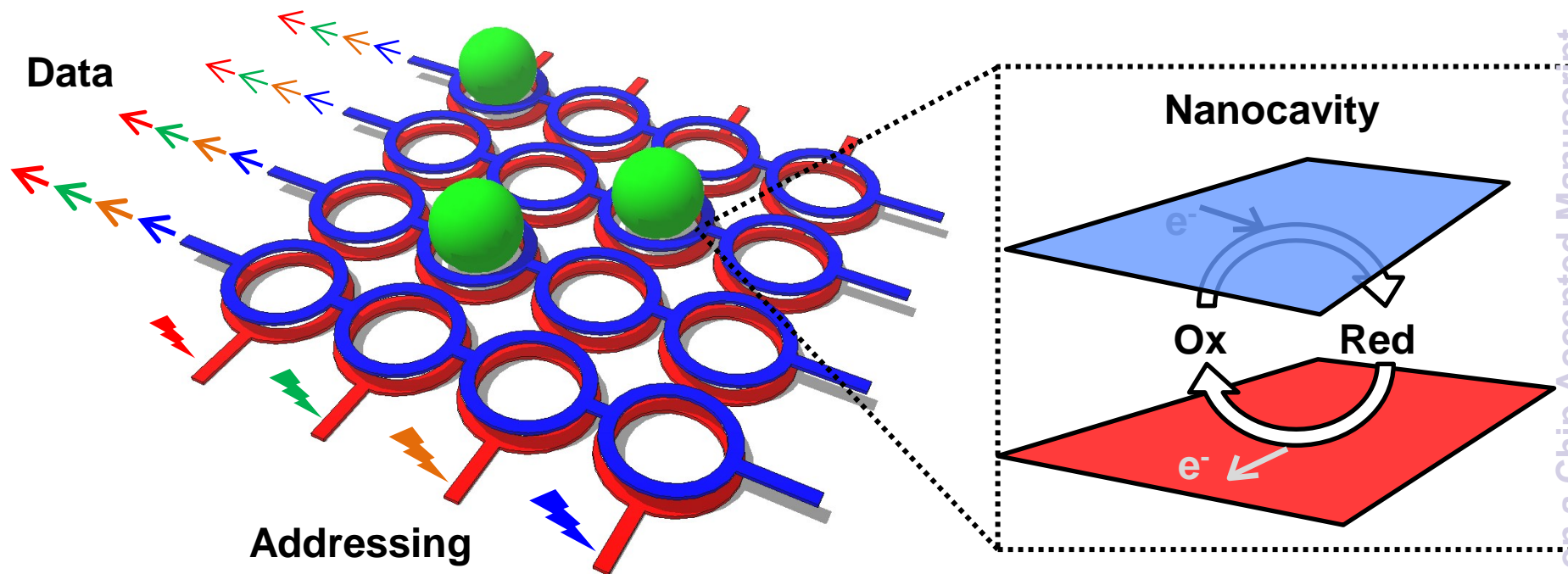
Figure 8



Lab on a Chip Accepted Manuscript

**Figure 9**





We developed an local redox cycling–based electrochemical (LRC-EC) device with nanocavities for multi-electrochemical detection of cell activity.